High-Fidelity Simulation of Dynamic Thermal Satellite Signatures with MuSES

Casey D. Demars[a], Corey D. Packard[b], David W. Tyler[a], and Christopher Rodgers[a]
[a]*The Tech7 Company*
[b]*ThermoAnalytics*

ABSTRACT

Thermal imaging phenomenology for space-domain awareness has benefits over conventional electro-optical imaging alone, potentially providing additional information about the operational state of target satellites. LWIR sensors also provide capability for daytime imaging, as demonstrated with the 3.6 meter telescope at the AMOS site on Maui, Hawaii. Detailed radiometric simulations with 3-D synthetic satellite objects can provide a valuable forward model for estimation problems; however, due to the complex computations required to simulate radiative transfer, development of satellite-focused thermal modeling and simulation has lagged similar tools developed for visible and SWIR sensors. Here, we demonstrate the use of MuSES to generate external temperature distributions for synthetic targets. MuSES simulates transient solar loading, thermal radiation from earth and to space, as well as conductive and radiative transport from internal heat sources such as electronics. Additionally, solar panels and battery cell charging and discharging can be realistically incorporated via coupled thermal/electric multi-physics solvers in MuSES. By attributing the synthetic target with the emissive properties of the materials at each surface facet, we can convert model temperature distributions to radiance maps. These maps allow radiometric signal levels in mid- and long-wave IR wavebands to be generated by simulating telescope and sensor effects. Using these tools, we demonstrate observation of the change in target surface temperature distributions and infrared signal levels due to an internal power source. We evaluate temperature distributions of a 3U CubeSat under different operating loads for multiple orbits, including low-earth and geostationary orbits in and out of eclipse. We also demonstrate the incorporation of thermal models into a high-fidelity radiometric environment for generating multi-spectral light curves.

1. INTRODUCTION

As the number of satellites and space debris increases and countries continue to weaponize the domain, it becomes more important to improve the detection, tracking, identification, and characterization of space objects. Continuous (24/7) space surveillance means overcoming such limitations as sky background and weather. Electro-optical telescopes and visible / near-IR sensors and space surveillance radars each have limitations, creating a need for complementary sensor technology. Further, satellite characterization – understanding the target's mission, material composition, vulnerabilities, capabilities, attitude and operational state – demands multiple approaches.

Characterization problems involving the operational state of a satellite are particularly well-suited to long-wave infrared (LWIR) measurements in a waveband typically dominated by physical temperatures. For example, estimates of surface temperature from LWIR data can be used to estimate how much power is being generated internally, from which inferences can be drawn about the satellite's payload. If the rate of cooling can be estimated from measured data, inferences can be made about external materials, vulnerability to directed energy or kinetic weapons, or payload age. Further, LWIR sensing can extend surveillance capabilities past the relatively short "terminator" periods when the satellite is illuminated by the sun against a dark sky. Finally, time-sampled temperature measurements – thermal light curves – can be used to estimate pose.

Numerous characterization focused applications using LWIR data for space-domain awareness (SDA) have been evaluated using the 3.6 meter Advanced Electro-Optical System (AEOS) telescope on Maui, Hawaii. Hall *et al.* (2006) [8] conducted observations of NASA's *Image* satellite with the AEOS LWIR imager to diagnose the operational status of the satellite after communication with the satellite was lost. Due to small temperature differences observed when the satellite was fully operational or in standby mode, the authors could not make a conclusion on the state based solely on the LWIR light curve. Hall *et al.* (2015) [9] conducted a controlled experiment with the Naval Research

Laboratory satellite *SpinSat* to assess the detection of firing Electrically-Controlled Solid Propellant (ESP) thrusters using LWIR light curves. Werth *et al.* [20] exploited the relatively low turbulence blurring at LWIR wavelengths to decrease multi-frame blind deconvolution processing time and improve reconstruction quality by fusing the object support constraint from LWIR with the visible-wavelength data.

Characterization belongs to a broad category of mathematical inverse problems. Typical of such problems, satellite characterization is generally ill-posed; multiple solutions fit the data, and no formal analytical solution exists. In lieu of viable formal solutions, predictions made by simulations using a rigorous, detailed forward model can be compared with measurements. Various approaches have been demonstrated for thermal modeling and analysis of spacecraft including analytical models [6] and specialized software packages [4, 10]. Thermal analysis is generally leveraged for satellite thermal control design to assess the probability that satellite components can withstand the extreme hot and cold conditions that will be experienced [1, 5]. While useful in assessing satellite thermal control, these approaches do not provide the temporal dynamics required for accurate thermal light curves that can be exploited for SDA characterization.

The SDA community has spent significant time and effort understanding how to exploit imaging and non-imaging measurements in VNIR and SWIR wavebands with notable success. Moreover, several efforts have been made to exploit spectroscopy and polarimetry for SDA applictions [3, 17, 18, 21]. The thermal regime, particularly LWIR, has remained underutilized due to the limited sensitivity of the sensors along with a lack of practical tools to understand the thermal dynamics occurring in the satellite. This work, demonstrated by Tech7 and ThermoAnalytics, looks to exploit unresolved infrared sensing (particularly LWIR) by creating an approach to incorporate LWIR data with state-of-the-art modeling and simulation. For both low earth orbit (LEO) and geosynchronous orbit (GEO), we use MuSES™ to predict the dynamic temperatures of a 3U CubeSat under varying loads throughout its orbit. Using a GEO example case, we demonstrate the ability to combine thermal results from MuSES with the KODOS simulation environment to generate multi-spectral signatures including visible, short-wave infrared (SWIR), and LWIR.

In this paper, we demonstrate an approach to simulate thermal signatures of resident space objects (RSOs) using the commercial software MuSES™. In Section 2 we discuss the KODOS high-fidelity radiometric simulation environment and its ability to generate realistic multi-spectral light curves. In Section 3 we describe MuSES and its capability to simulate accurate thermal signatures of RSOs over various orbital regimes and different operating conditions. We also present the concept of an emissivity distribution function (EDF) that represents the anistropic 3D signature of emission from a target. Similar to the bi-directional reflectivity function which represents light scattering from a surface given the incident and exitant angles, the EDF represents the directional emissivity distribution. Section 4 details the different orbital scenarios and operating conditions of the simulated RSOs. Section 5 presents results including coupled thermal-electrical simulation predictions, subsequent LWIR signatures and multi-spectral light curves. In Section 6 we present a summary and conclusions.

2. KODOS AND DIRSIG

Tech7 has developed a powerful simulation environment named KODOS to simulate electro-optical observations of space and ground objects. Rochester Institute of Technology's DIRSIG [2] serves as KODOS' radiometric core, generating 3D radiance maps of synthetic targets over the spectral range of 0.4 to 20 microns. DIRSIG has capabilities for polarimetry, LIDAR and RADAR.

DIRSIG has various built-in heat transfer solutions for predicting surface temperatures and LWIR radiances; however, as we will discuss, MuSES allows us to integrate electronics, batteries, PVs and other active elements, allowing full control over the simulation heat dynamics. The integration of satellite components in MuSES also means specific scenarios, such as internal component failures, can be analyzed.

KODOS has been developed to accommodate ground, air, and space sensing platforms, and space objects can span different orbital regimes (LEO, MEO, GEO, and cis-lunar). Synthetic targets can be manipulated in KODOS to simulate position and attitude maneuvers, model articulation, and object ejection during an observation. KODOS leverages a built-in geometry engine to calculate the geometry of the scene and appropriately generate simulations that are performed in a parallel environment.

Simulations of both existing and conceptual sensors can be integrated with KODOS by developing the appropriate optics and detector effects model (ODEM). Because KODOS itself is written in Python, ODEMs can be written

in numerous programming languages, including Python, MATLAB, C++, IDL, or Fortran. KODOS will then send completed DIRSIG radiance maps to the ODEM through a language interface to generate simulated data from the sensor, complete with optical or electronic effects included in the ODEM. Example ODEMs currently integrated with KODOS include a framing-array imaging camera, a full-Stokes polarization imager, a time-delay and integration (TDI) imager, a spectrometer, and a spectro-polarimeter.

3. MuSES

MuSES™ is an export-controlled commercial heat transfer and EO/IR sensor radiance prediction software developed by ThermoAnalytics that uses a numerical, finite volume method based on first principles physics to solve energy balance for heat transfer due to conduction, convection, and radiation. MuSES is considered the gold-standard for high-fidelity U.S. Army ground vehicle simulation, and is used by domestic and ally defense agencies to predict the signature of high-value tracked and wheeled vehicles, maritime vessels, human personnel, manned and autonomous rotary and fixed-wing aircraft. The thermal-only version of MuSES (referred to as TAITherm™) is used by many major automotive OEMs around the world, as well as in other industries like architecture, aerospace, manufacturing and textiles. MuSES has been validated [11, 16] under contract for US Army, US Navy and Department of Energy applications, and several DoD groups accept MuSES prediction results as a method for demonstrating signature management (SIGMAN) compliance against EO/IR signature requirements. Past examples of this include DDG 1000 (2005), Future Combat Systems (FCS, 2004-2007), Joint Light Tactical Vehicle (JLTV, 2008-2016) and the XM30 Mechanized Infantry Combat Vehicle (formerly known as the Optionally Manned Fighting Vehicle, 2022-present). MuSES is used by all DoD agencies, the intelligence community, several National Labs and many US Department of State-approved foreign groups.

Thermal simulation with MuSES requires a 3D surface mesh (and volume mesh, where desired) to describe the system geometry (example shown in Figure 1). This mesh is used for automatic view factor calculation, lateral and vertical conduction via automatic nodal network generation, radiative and convective (when applicable) heat transfer. The depth of each portion of the surface mesh is handled virtually by a user-supplied thickness that allows analysts to study the impact of surface thickness without needing to regenerate the 3D mesh. Element-to-element and/or part-to-part thermal links can also be defined to conduct heat via a path other than the automatic mesh-based method. Thermal material properties from a database are applied to each component to characterize the transient thermal response to supplied boundary conditions and mission profiles. Optical properties (e.g., albedo and thermal emissivity) are specified for each surface to govern radiation exchange, and internal heat sources can also be defined with a variety of sophistication levels depending on user requirements. Physical temperatures are calculated for all elements at each discrete timestep in the simulation using these model attributes and supplied/calculated transient boundary conditions.

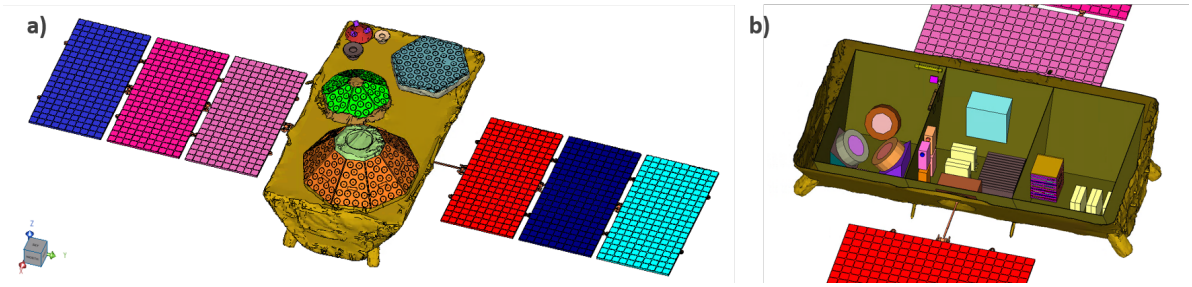

Fig. 1: Example of a Globalstar satellite screenshot exported from MuSES, with part/feature edges shown but with the element mesh suppressed for clarity. The different colors correspond to distinct parts in the simulation model; exterior surfaces are depicted in Panel a), while Panel b) portrays interior components.

These boundary conditions can be calculated by the MuSES software, supplied by the user or a combination of these two approaches. Taking a complex LEO path as an example, KODOS can supply MuSES with a variety of orbital and environmental parameters based on a TLE (two-line element) set. These include earth-centered earth-fixed (ECEF) satellite positions which specify X-Y-Z location relative to the Earth and Sun, satellite attitude quaternions to control orientation with respect to the Earth, and solar angle which is used to correctly position the sun. Together, these boundary conditions are used to automatically position the Sun, satellite and Earth correctly with respect to each other

for thermal simulation purposes. However, for a simpler GEO path and a non-tumbling payload, MuSES can calculate solar position, solar angles and eclipse times based on simple user inputs such as latitude, longitude and satellite altitude above the Earth. This multiplicity of approaches for supplying dynamic orbital boundary conditions provides flexibility and control to the analyst.

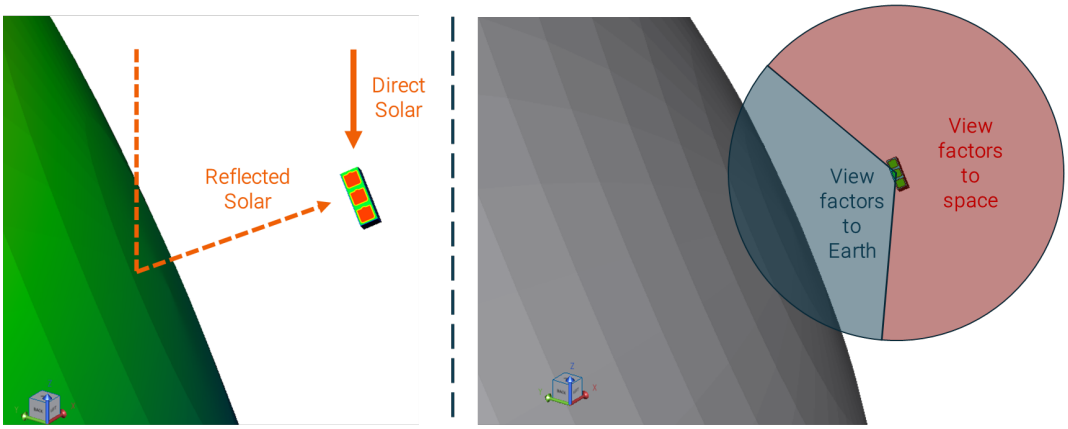

Fig. 2: Illustration of thermal boundary conditions that serve as the primary external environmental forcing functions for satellite temperatures. On the left, direct and reflected solar radiation is depicted with solid and dashed arrows, respectively. At right is a portrayal of thermal radiation exchange (via automatically-calculated view factors) between the satellite, Earth and space.

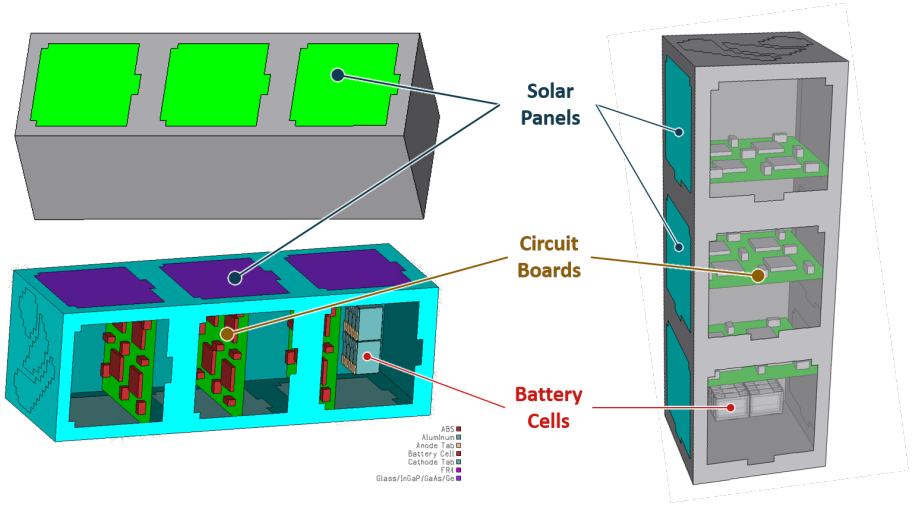

Fig. 3: Example of a 3U CubeSat with solar panels and internal components exposed, including circuit boards and battery cells. Exterior geometry (upper left) with solar panels highlighted, parts colored by material (lower left), and both interior/exterior geometry shown with primary components indicated (right).

MuSES is capable of integrating batteries into thermal simulations via a coupled thermal/electrical multi-physics solution [12, 13, 14]. The current through each battery cell is dependent upon the electrical boundary conditions and the state of the cell, including the temperature of the cell and the depth of discharge. The heat generated in a cell is modeled with both irreversible (Joule heating) and reversible (entropic heating) terms, and is dependent on the current through the cell and the temperature-dependent state of the cell. The thermal model uses these generated heat rates to calculate the evolution of the battery cell temperatures. MuSES is also capable of integrating photo-voltaic (PV) panels into thermal simulations via a coupled thermal/electrical multi-physics solution [7]. The PV electrical calculations are performed at the conclusion of each thermal simulation timestep, and photogenerated energy production can be calculated by using one of two methods. Figure 3 illustrates the incorporation of solar panels (whose efficiency is solar

angle-dependent and temperature-dependent), circuit boards (which represent the electrical system load), and battery cells (which are charged by the PV panels and discharged by the circuit boards).

The solar panels and battery cells can be represented several ways, depending on the required fidelity and information available to the simulation engineer. One method is to use an equivalent circuit, shown in Figure 4. As mentioned earlier, MuSES solves both the thermal and electrical problems concurrently. This results in accurate results for PV efficiency and harvested solar energy, battery current/power/SoC (state of charge) information, as well as temperature predictions for both of these components (and others including the circuit boards). These physical temperatures serve as the necessary foundation for EO/IR sensor predictions in thermal wavebands (e.g., MWIR and LWIR), which we explore in this work.

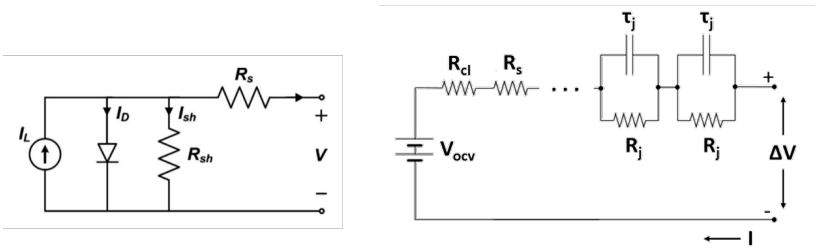

Fig. 4: These diagrams illustrate the equivalent circuit approaches for PV panels (left) and battery cells/packs (right) that can be employed by MuSES.

Beyond this, design temperature requirements can be supplied to MuSES to visualize components whose temperatures may stray outside their desired thermal envelope and exceed their specified operating range at some point during an orbit. Figure 5 depicts a representative example of this technology.

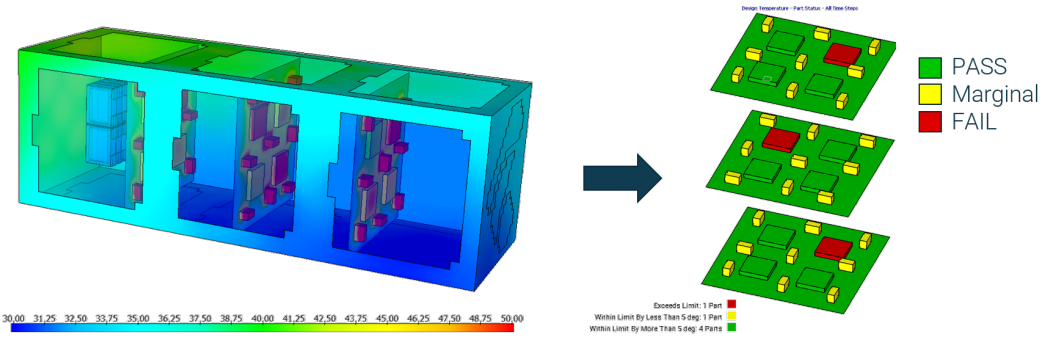

Fig. 5: Example results for a 3U CubeSat including interior/exterior surface temperatures (left, degrees Celsius) and with electronics pass/fail indications shown based on maximum design temperature constraints (right).

Finally, multiple MuSES runs can be used to calculate the emissivity distribution function (EDF) at any desired resolution. The EDF is a two dimensional construct, giving the radiance in $W/m^2/sr$ of a point source at a given sensor azimuth and elevation. The EDF is temporally dependent on both incident radiation and any internal loads of the target. The EDF can be exploited to understand the radiance signature based on the state of individual components and the object orientation in space. Example EDF results are shown in Section 5.3.

4. SCENARIOS

In this work, we explore different orbits and operating conditions to study the impacts they have on the thermal signature of a satellite. A general sun-synchronous orbit has an altitude between 500 and 2000 kilometers and passes near the poles, moving between being sunlit and eclipsed by Earth's shadow. Shadowing in GEO also occurs around the solstices when the sun is aligned with the equatorial plane. Passing in and out of shadow changes the temperature of the satellite while impacting incident solar radiation falling on the PVs. When the solar panels are not sunlit and collecting solar radiation, measures to reduce power consumption may be needed which in turn effect the electronic

load, the dissipation of the battery, and the efficiency and throughput of the PVs. These factors contribute to the overall thermal distribution across the satellite.

4.1 Description of 3U CubeSat

This work focuses on a 3U CubeSat satellite, so a brief description of the payload in question is appropriate here. A 3U CubeSat has exterior dimensions of 30 cm x 10 cm x 10 cm, and we equipped three of the large sides (faces labeled in Figure 6) with triple-junction GaAs solar panels totaling just over 181 cm^2 per side. The solar panels have a solar absorptivity of 0.63 (which includes the nominal stated PV efficiency of 28%) and a thermal emissivity 0.89. This is in contrast to the shiny metallic finish on the rest of the payload; the non-PV surfaces have a solar absorptivity of 0.50 and a very low thermal emissivity of 0.05. These values are used by MuSES for its dual-band radiation solver; EO/IR renderings employ spectral surface descriptions (i.e., wavelength-dependent emissivity, diffuse and specular reflectivity values) and the Sanford-Robertson BRDF model.

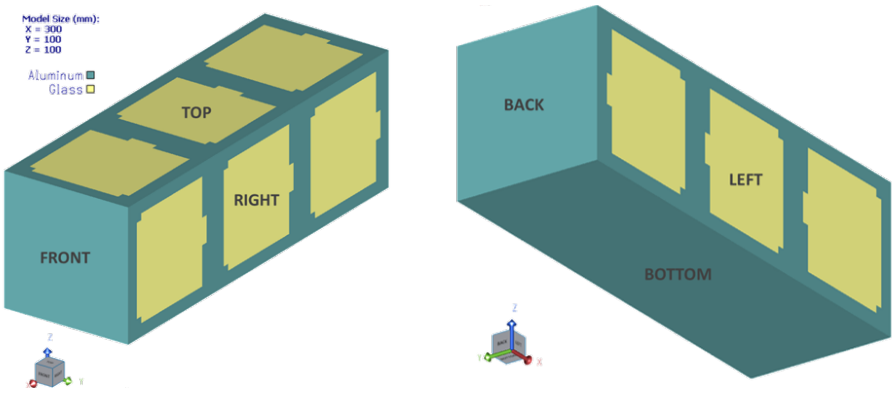

Fig. 6: Illustration of 3U CubeSat geometry with the six faces labeled and the PV panels (present on three of the six faces) shown in yellow.

The nine solar panels (three on each of three PV-equipped sides) harvest energy from the sun with a temperature-dependent and incident-angle dependent efficiency that is calculated during the dynamic simulation. This absorbed solar energy, when present outside the eclipsed region of the orbit, is used to charge the internal battery pack shown in Figure 3. Eight (8) battery cells, each with a 0.375 A-hr capacity, are configured in a 4S2P topology. These battery cells are used to power the internal electronics (three circuit boards, shown in Figure 3 and Figure 5) which together require three (3) Watts of power during satellite operations. A battery management system (BMS) is employed to enforce charge/discharge limits when the state-of-charge (SoC) is above 90% or below 10%.

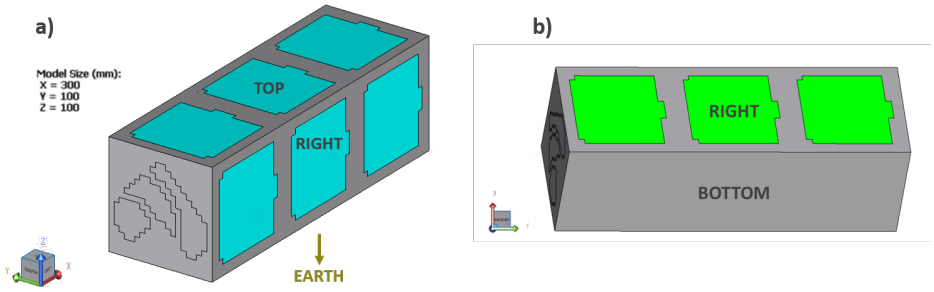

Fig. 7: Illustration of 3U CubeSat geometry along with MuSES coordinate system shown for reference. The reflective metallic surfaces are depicted in gray, while the PV panels are highlighted in cyan and green. Panel a) depicts satellite attitude for the LEO and simple GEO scenarios, while Panel b) portrays the orientation of the satellite from the Earth's perspective during the GEO path based on the GOES-17.

Panel a) of Figure 7 shows the orientation of the satellite, with respect to the Earth, for the LEO and simple GEO scenarios described in Section 4.2 and 4.3; the Earth is "below" the satellite in the -Z direction. In the simple GEO

scenario, the path of the sun relative to the satellite body reference frame traces a circle in the Y-Z plane, primarily illuminating the four long rectangular CubeSat sides (three of which are equipped with solar panels). For the more complex GEO scenario based on the GOES-17 and described in Section 4.4, the CubeSat 3U geometry seen in Panel b) of Figure 7 is shown from the perspective of Earth; both a PV-equipped side and a side sans solar panels are aimed at the Earth.

4.2 Scenario 1: 3U CubeSat in LEO

This scenario is for a sun-synchronous LEO orbit using the two-line element for a Space-X Starlink satellite given as

```
0 STARLINK-2461
1 48428U 21040A   22305.35754059  .00001394  00000-0  11247-3 0  9998
2 48428  53.0533 282.8707 0002250  51.9033 308.2159 15.06402681 83306.
```

The orbit was propagated using the Simplified General Perturbations (SGP4) model [19] starting at 2022-11-01T00:00:00 for 320 time samples with 60 second sampling. The orbital path is shown in Figure 8 (a) along with the altitude shown in Figure 8 (b) and the eclipse periods shown in Figure 8 (c).

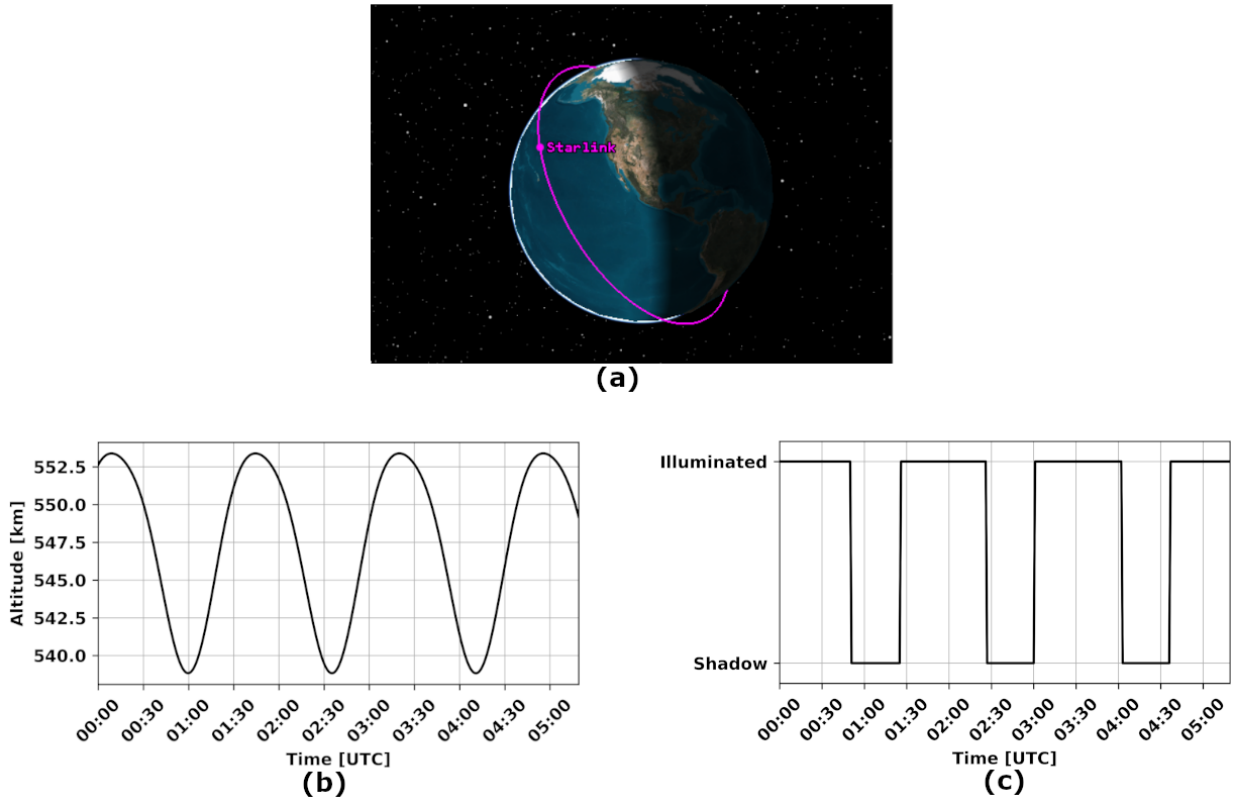

Fig. 8: (a) - Path of the Starlink-2461 Orbit in the earth centered inertial coordinate frame with shown with Earth's terminator shadow. (b) - Altitude of the orbit over the simulated time interval. (c) - Status of object being illuminated or in shadow over the simulated time interval.

4.3 Scenario 2: 3U CubeSat in simple GEO

In this general scenario, the path of the sun relative to the satellite body reference frame in MuSES (shown in Figure 7, left) traces a full circle in the Y-Z plane over a 24-hour period. This primarily illuminates the four long rectangular 3U CubeSat sides, three of which are equipped with solar panels. The satellite is positioned at an altitude of 35,786 kilometers and is positioned such that its large sans-PV satellite face is directly facing the Earth. A three-axis stabilized attitude is assumed, where the view factors from the various satellite faces to the Earth and space are constant and only the solar illumination angle and altitude-dependent eclipse is time-dependent. MuSES uses a dynamic solar position

relative to the satellite geometry to simulate an orbiting payload, and excludes solar loading entirely during the brief orbit segment when the payload is eclipsed.

4.4 Scenario 3: 3U CubeSat in GOES-17 GEO

This scenario is for a geosynchronous orbit during eclipse season using the GOES-17 TLE given as follows:

```
0 GOES 17
1 43226U 18022A   22241.66234375  .00000098  00000-0  00000-0 0  9994
2 43226   0.1013 278.8974 0000226 228.5100 291.5628  1.00272724 16507.
```

The orbit was propagated using SGP4 starting at 2022-09-19T07:00:00 for 320 time samples with 60 second spacing. The orbit is shown in Figure 9 (a) where it is illustrated that the satellite is in Earth's shadow. The eclipsed and sunlit periods are shown in Figure 9 (b); the eclipse period starts around 08:30 UTC and last slightly longer than one hour until just after 09:30 UTC.

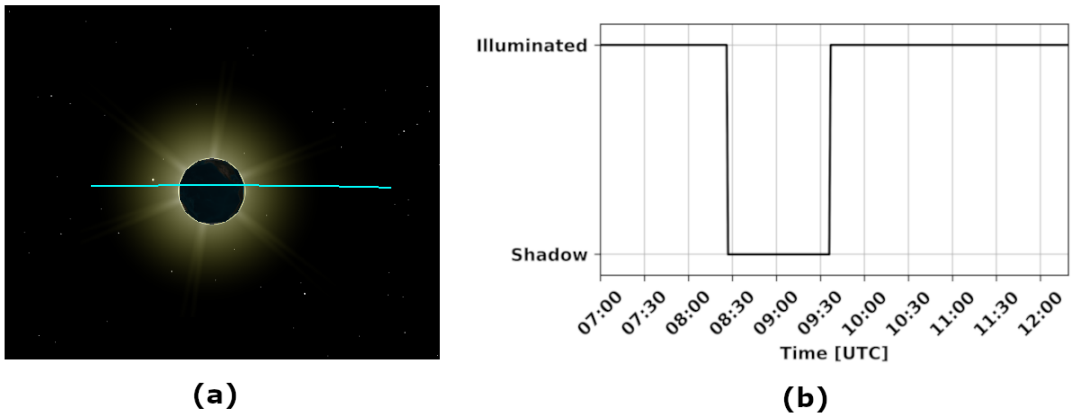

Fig. 9: (a) Path of the GOES-17 Orbit in the earth centered inertial coordinate frame with reference to the earth and sun. (b) Status of object being illuminated or in shadow over the simulated time interval.

A three-axis stabilized attitude is assumed, so only the solar illumination angle and eclipse are time-dependent. The satellite is positioned with two of its large faces aimed at the Earth. MuSES calculates the dynamic solar position relative to the satellite geometry for the user-specified latitude and longitude, excluding solar loading entirely during the brief orbit segment when the payload is eclipsed according to Figure 9 (b).

For this scenario, the "left" face of the satellite (one of the three sides which has PV panels on it) and the "bottom" of the satellite (which lacks solar panels) are the primary sides of the orbiting payload that face the Earth (see the geometry shown in Figure 7, right, which shows the satellite from the Earth's perspective). In this scenario, the path of the sun relative to the satellite body reference frame in MuSES traces an arc that is primarily "underneath" the satellite over a 4-hour period. This results in the illumination of the "left" face which is equipped with a solar panel on most of its surface, the bottom (sans-PV) face and the small end faces which also lack solar panels. This means that surfaces visible from Earth, shown in Figure 7 (right), are the primary solar-illuminated faces.

5. RESULTS

5.1 Results for Scenario 1: 3U CubeSat in LEO

An orbit with an altitude around 550 km has a period of approximately 96 minutes, so a 320 minute segment encompasses just over 3 complete orbits around the Earth. The results of the thermal-electrical coupled MuSES simulation for the Starlink-based LEO scenario are portrayed in Figure 10. The six panels illustrate various related battery and PV panel quantities, calculated by MuSES, with the thinner red lines representing the "3W Load" case and the thicker black lines indicating the "No Load" case.

Panel a) shows the state-of-charge (SoC) of the battery packs, which both begin their orbits charged to 50% of their total capacity. In the "No Load" case, the presence of solar illumination charges the battery cells quickly in the absence of an electrical load on the battery pack, and once the battery pack exceeds 90% the battery management system (BMS) disables further charging. This is evident in Panel d) as well, where the "No Load" current drops to 0 once the SoC reaches 90%. The battery pack temperature (Panel b) oscillates during the orbit due to variations in available PV-harvested power (Panel e), which in turn depends on temperature-dependent panel efficiency (see Panel c) and Panel f) for PV temperature and efficiency, respectively).

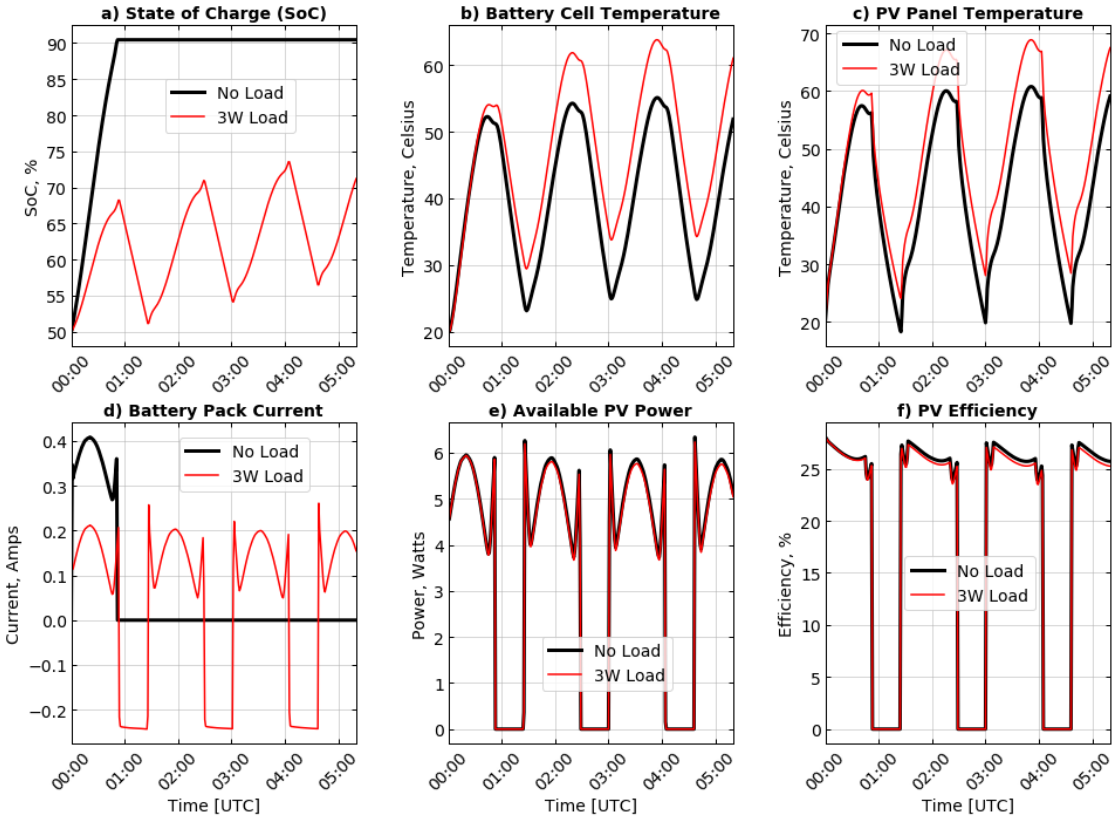

Fig. 10: Battery and PV panel results for the 3U CubeSat in a LEO based on a Starlink TLE.

For the "3W Load" case, the battery pack temperature exceeds that of the "No Load" case; see Panel b) for the average battery cell comparison. As in the "No Load" case, the available PV power oscillates with several eclipse-induced outages evident in Panel e). A slight decrease in solar power can be seen due to the temperature-based efficiency discrepancy; Panel f) shows PV efficiency, but the more significant increase can be seen in the PV temperature displayed in Panel c). Both the increased battery pack temperature and increased PV panel temperatures are related to the 3W internal electronic load, and the corresponding impact on pack charge/discharge current and SoC are indicated in Panel d) and Panel a). Each eclipse period requires a discharge of the battery pack to sustain the 3W load, and this is indicated by reductions in SoC and negative pack current values (i.e., battery discharge). Once each eclipse ends and

more than 3W of solar power are available to the system, the pack current become positive (indicating charging) and the SoC values rise.

Beyond exterior and interior temperature predictions, MuSES was used to predict transient satellite hardbody signatures from the perspective of a virtual LWIR sensor viewing the orbiting payload from the perspective (direction) of Earth. The results of this LWIR signature study are shown in Figure 11. In the upper-left, Panel a) displays a comparison of sensor radiance images representing hardbody signatures at 03:45 UTC. The same comparison, in apparent temperature units, is shown in Panel b) in the lower-left. A transient signature comparison for all times in the dynamic orbital simulation is shown in Figure 11 (right).

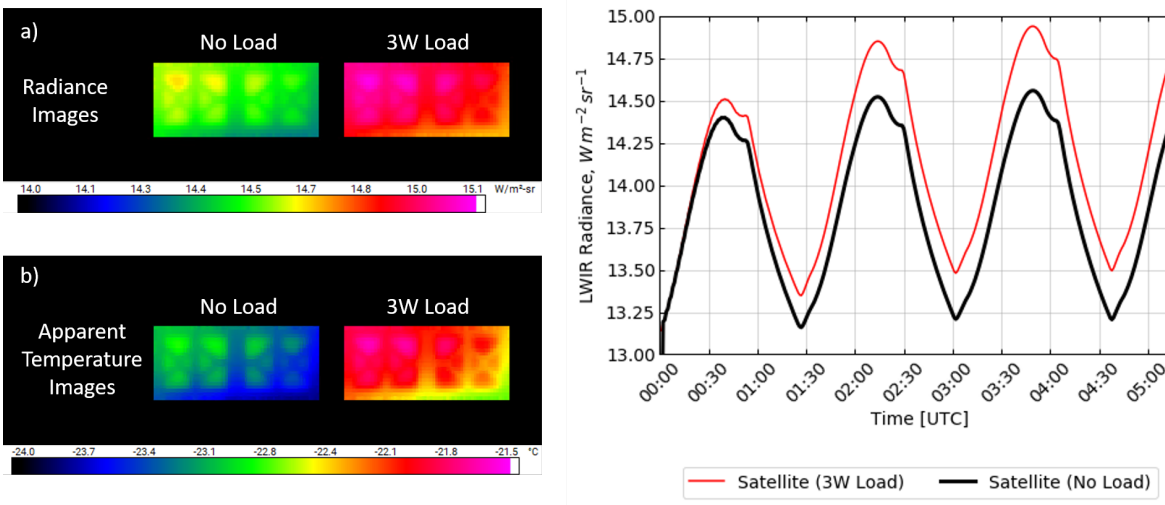

Fig. 11: LWIR results for the 3U CubeSat in LEO where the average satellite signature, from the Earth's perspective, is shown for two electronics loads. In the upper-left, Panel a) compares well-resolved radiance images of the "No Load" satellite with that of the "3W Load" satellite, both at 03:45 UTC. Panel b), lower-left, shows the same comparison in apparent temperature units. The line plot (right) shows the pixel-averaged predicted transient signature of a satellite with internal circuit boards drawing 3W of power from a battery charged by the solar panels (thin red line labeled "3W Load") compared to the signature of a satellite whose internal components are inactive (thick black line labeled "No Load").

Note that while the internal and external thermal differences between the "No Load" and "3W Load" satellites are evident from Panel b) and Panel c) in Figure 10, respectively, the increase in LWIR hardbody signature (due to the internal 3W load) is less evident in Figure 11 than it might otherwise be. While the PV panel temperature increases by up to 10°C due to a 3W load, the LWIR signature increases by only 0.25 W m^{-2} sr^{-1}. This is because a very low LWIR emissivity (for all non-PV panel surfaces) was used for signature prediction purposes, resulting in the thermal hardbody differences being masked by very significant reflections of the surrounding environment (e.g., space, Earth, Sun). This represents a worst case scenario for a LWIR remote sensor commissioned with observing an increase in radiance due to internal heating, and suggests predicted observations of solar panel-equipped CubeSat faces might be even more interesting. This is addressed in Section 5.2, where additional views of the satellite are presented.

5.2 Results for Scenario 2: 3U CubeSat in simple GEO

The results of the thermal-electrical coupled MuSES simulation for the simple GEO scenario are portrayed in Figure 12. The six panels illustrate various interconnected battery and PV panel quantities, with the thicker black lines indicating the "No Load" case and the thinner red lines representing the "3W Load" case. Panel e) shows the available PV-harvested solar energy, which varies between 0W (during the eclipse at the center of the orbit) and approximately 9.5W at the peak; this should be understood in context, as the constant electronic load of the activated satellite is 3W. The available solar-sourced power is impacted by PV panel efficiency, shown in Panel f), which in turn depends on solar angle of incidence and panel temperature (as seen in Panel c, this is higher for the "3W Load" case, which reduces PV efficiency).

Panel a) shows the "3W Load" satellite beginning with its battery packs 50% charged, and the surplus solar illumina-

tion immediately begins charging the battery cells (indicated with a thin red line) until they reach nearly-full capacity in less than an hour. As the available solar power shown in Panel e) drops below 3W, the battery pack must supply the necessary energy which results in a discharge current (see the thin red line in Panel d), which indicates discharge with negative values and charge current with positive values). Once the available PV power once again exceeds 3W, the battery pack current switches polarity to positive (charging status), and when the battery cells exceed 90% charge level the battery management system (BMS) disables further charging.

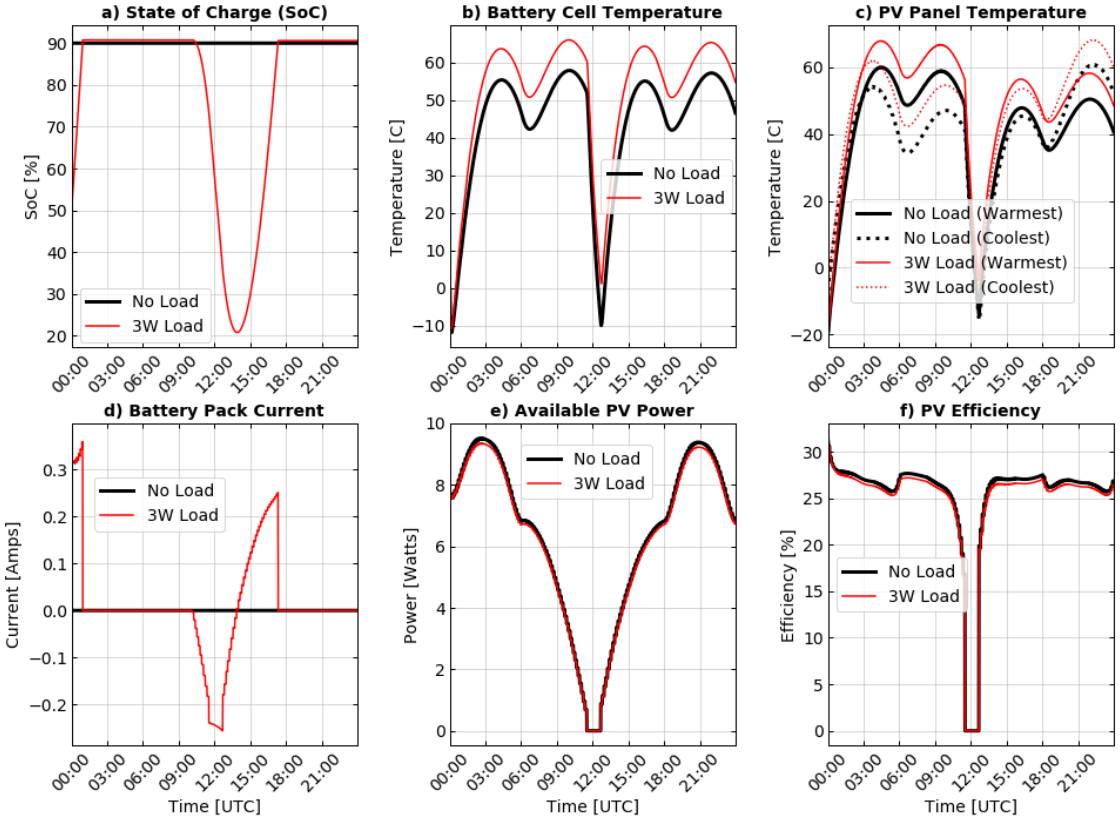

Fig. 12: Battery and PV panel results for the 3U CubeSat in a simple GEO dynamic orbit. The path of the sun illuminates the four large sides of the satellite, three of them equipped with solar panels.

Meanwhile, for the "No Load" payload which begins its orbit 90% charged, the lack of an electronic load means the battery cells stay charged for the duration of the orbit (indicated with a thick black line in the various panels). SoC thus stays constant at 90%, the battery pack current is flat at 0 amps, and the resultant battery cell and PV panel temperatures are generally cooler than with the "3W Load" case. The solar panel temperatures correlate with incident solar flux, as do the battery cell temperatures due to the thermal link between the satellite interior and exterior.

Figure 13 depicts both the "No Load" and "3W Load" satellites from two sensor perspectives at 10:00 UTC, looking down on the Earth ("from above") and looking up from the Earth ("from below"). Radiance differences are evident but are more significant when the satellite is viewed from above; this is due to the higher emissivity of the solar panels when compared to the other highly reflective metallic surfaces. These perspective-dependent satellite radiance values suggest that the difference between the hardbody signature of an active payload and one that is inactive is likely more discernible from some sensor angles than others. This is explored further in Section 5.3.

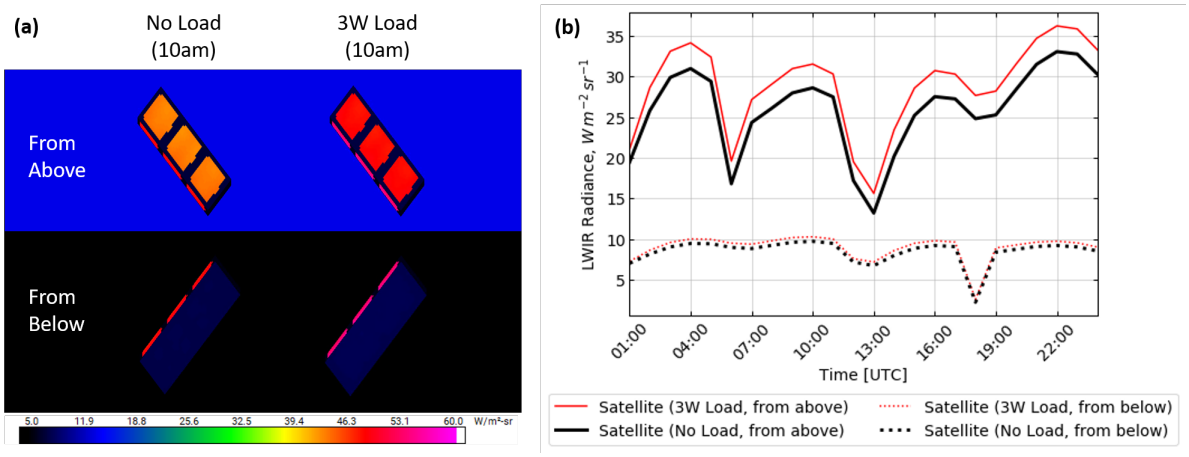

Fig. 13: (a) MuSES-rendered LWIR images of the 3U CubeSat satellites ("No Load" and "3W Load") from both above and below, at 10:00 UTC. (b) Transient satellite-averaged LWIR results from those two sensor perspectives, including from (almost) the Earth's perspective (labeled "from below") and towards the Earth (labeled "from above"). The predicted signature results shown are for two orbiting payloads, one with an internal 3W power load (red, labeled "3W Load") and another with inactive internal components (thick black, labeled "No Load").

5.3 Results for Scenario 3: 3U CubeSat in GOES-17 GEO

It is important to understand the connection between dynamic orbital boundary conditions, subsequent thermal simulation results and – ultimately – LWIR radiance from the perspective of a virtual sensor. To illustrate this, Figure 14 shows a trio of MuSES results for one particular time-step in a multi-hour transient simulation. First, the primary environmental forcing function, absorbed solar flux, is depicted (left) for the 08:00 UTC time-step. The colors here indicate the level of absorbed solar radiation, and correspond to the false color palette shown below the colored geometry. Note that one large side with solar panels is illuminated while the other (visible) 300 cm^2 side and the (visible) adjacent small side both show an absence of absorbed solar radiation. Shown in the center of Figure 14 is the corresponding 08:00 UTC thermal solution, where the impact of previously-stored energy, external boundary conditions and internal heating is depicted. The colors here represent physical temperatures corresponding to exterior surfaces and interior components based on the false color palette directly below the results-colored satellite geometry. The final image in Figure 14 (right) shows the LWIR diffuse radiosity solution for 08:00 UTC, which assumes grey body Lambertian surfaces and uses physical temperatures, thermal emissivities and a simple environmental model to precompute the diffuse radiance emitted by object surfaces. This solution is an approximate signature prediction that lacks important aspects such as directional reflections (e.g., solar/lunar glints), atmospheric attenuation and path radiance, directional spectral sky gradients and BRDF effects. These things (and more) are all considered during the final (validated) EO/IR rendering pipeline that results in sensor radiance predictions; the diffuse radiosity solution is merely an approximation that expedites signature renderings by precomputing some attitude-invariant quantities.

The results of the thermal-electrical coupled MuSES simulation for the GOES-17 scenario, portrayed in Figure 15, tell an interesting story. The six panels illustrate various interconnected battery and PV panel quantities, with the thicker black lines again indicating the "No Load" case and the thinner red lines representing the "3W Load" case. Panel a) shows both payloads beginning with their battery packs 50% charged, and solar illumination immediately begins charging the battery packs. In the "No Load" case, once the battery is 90%+ charged the BMS disables further charging, and the lack of an electrical load means the SoC remains fully-charged for the remainder of the orbit segment. For the "3W Load" case, the eclipse (which begins around 08:30 UTC) requires the battery to begin discharging to supply the necessary electrical power, but the conclusion of the eclipse (a little after 09:30 UTC) means the energy harvested by the PV panels resumes battery charging once more (indicated by an increasing SoC), until around 12:00 UTC when the available PV power falls below 3W and the battery must begin supplementing power. The charge/discharge current (shown with positive and negative current values, respectively) shown in Panel d) aids in understanding the SoC curves. The "No Load" current (shown in black) drops to zero once the battery is fully charged, while the "3W Load" case shows a short charge period (when available PV power exceeds the 3W load) followed by a brief discharge (during the eclipse). After this, charging results once the eclipse is over, but when the available PV

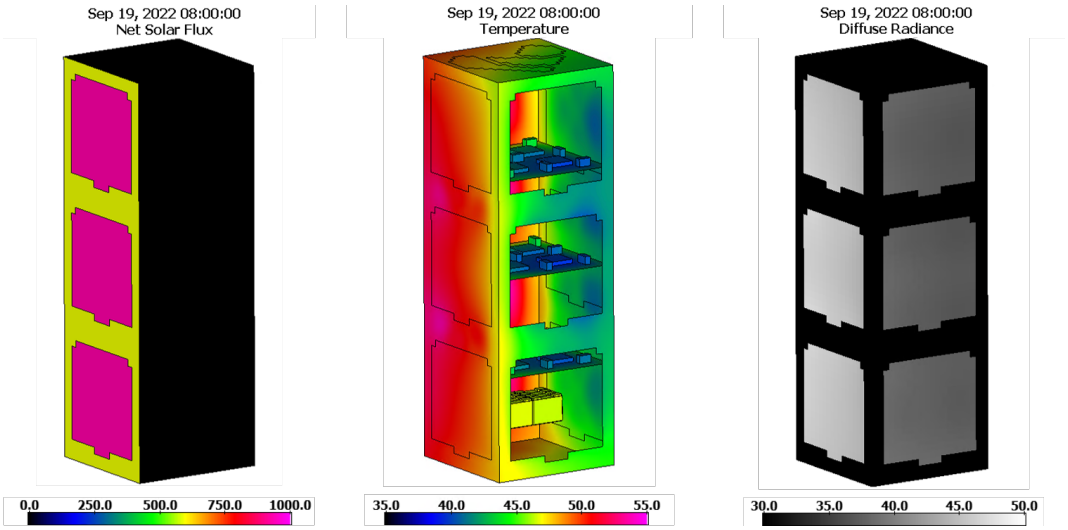

Fig. 14: Simulation results for the 3U CubeSat including absorbed solar flux (left, in W/m^2), surface temperatures (center, in degrees Celsius) and LWIR diffuse radiosity (right, W/m^2-sr). In the central (temperature) illustration, some of the PV panels are hidden for a clearer view of the internal electronic temperatures.

power drops below 3W (around 12pm) the battery pack current goes from positive (charge) to negative (discharge).

Panel b) shows the battery cell temperature which begins at 20°C and rises (during the sunlit portion of the GEO segment) to between 50°C and 60°C around 8:30am (depending on if the 3W load is present or not, shown in red and black, respectively). The lack of sunlight during the eclipse reduces the battery pack temperature to 0°C (or below) until the orbiting payload emerges from Earth's shadow and the battery pack warms once more. Note that battery cell temperatures are higher when the 3W load is supplied by the battery pack. Panel c) shows the PV panel temperatures for the warmest and coolest of the three satellite sides, for both the "No Load" (black) and "3W Load" (red) cases. The solar panel temperatures correlate with incident solar flux, as do the battery cell temperatures since there is a thermal link between the satellite interior and exterior, and the temperatures are generally higher for the "3W Load" case.

Panel e) shows the PV-harvested solar energy available to the satellite, which is dependent on both the presence of sunlight (the same for both the "No Load" and "3W Load" cases) and the efficiency of the solar panels. The related PV efficiency, shown in Panel f), is dependent on solar incident angle (the same for both cases) and panel temperature (higher for the "3W Load" case) seen in Panel c).

Thermal model results from MuSES were exported and used in the KODOS environment to generate simultaneous multi-spectral light curves in the visible, SWIR and LWIR bands. Integrated radiance values generated by KODOS in the multi-spectral bands are shown in Figure 17. Whereas previous radiance values have been in average pixel radiance, these values are the sum of radiances for all pixels subtended by the 3U CubeSat. The eclipse period starts around 08:30 UTC for which the radiance in the Sloan and Mauna Kea filters vanishes until the object comes out of eclipse just after 09:30 UTC. During the eclipse period, the LWIR radiance for the two operating conditions decreases as the object is shadowed and begins to cool. Over the eclipse duration, both of the LWIR radiances fall to under 40% of the radiance at the start of the eclipse. The visible and SWIR bands rely on reflected illumination; therefore, targets can't be detected during the eclipse period in these bands. The LWIR radiance shown for the two operating conditions decreases as the object is shadowed and begins to cool. These results, which combine the thermal results of MuSES with KODOS, demonstrate the capability to generate multi-spectral light curves which can be used to perform analysis in both the reflective and emissive spectral bands.

Shown in Figure 18 are EDF results for the GOES-17 scenario at 11:00 UTC. The EDF for the "3W Load" case shown is shown in Figure 18(a) while the EDF for the "No load" case is shown in Figure 18(b). The EDF peak occurs near the top-half center of the distribution which represents the NADIR face of the 3U CubeSat that is normal to the sunlight. This makes sense geometrically because after the eclipse the solar phase angle is small and the NADIR face is mostly orthogonal to the solar direction. The bright pixel just right of center is attributed to the reflected solar radiation from

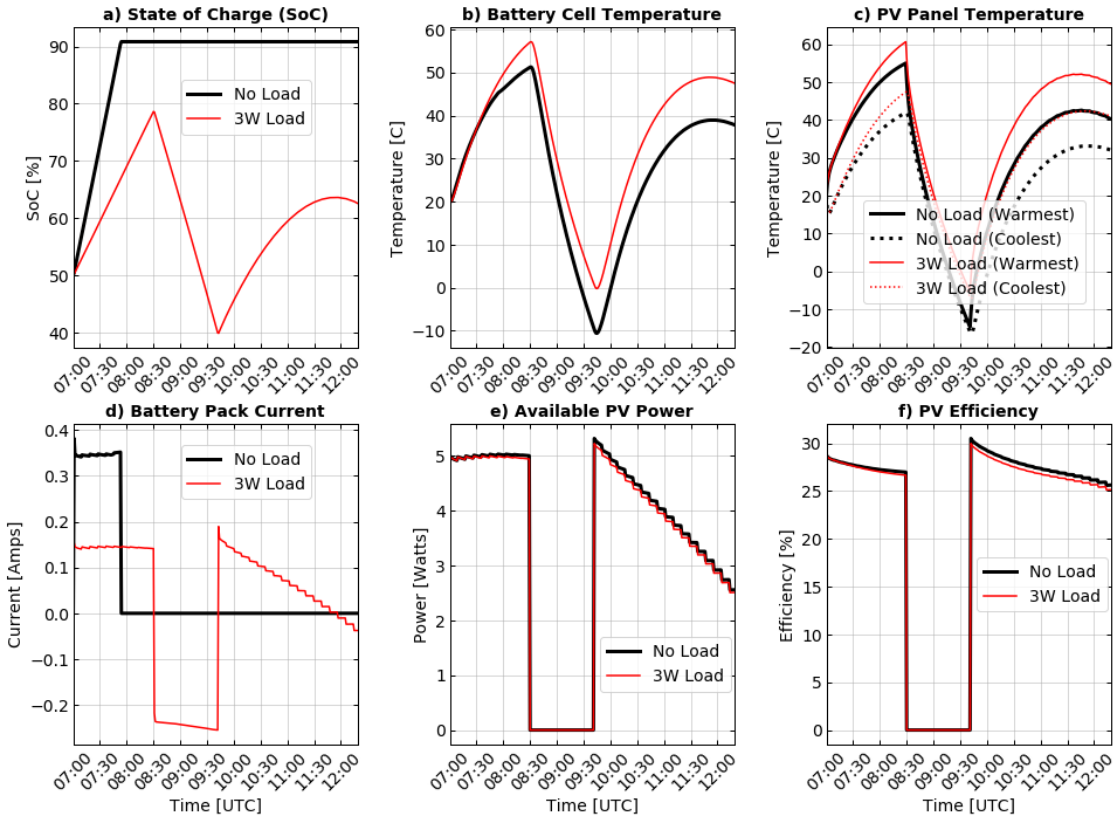

Fig. 15: Battery and PV panel results for the 3U CubeSat in a segment of the GOES-17 GEO.

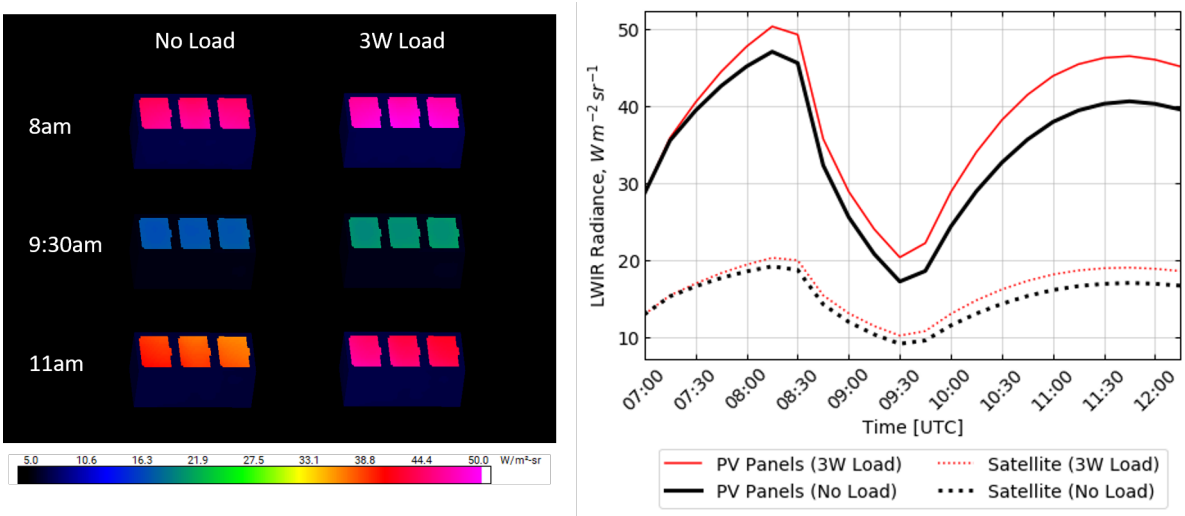

Fig. 16: Transient LWIR results for the 3U CubeSat where the average satellite signature and solar panel signature, from the Earth's perspective, is shown for two electronics loads. Predicted signature results from the satellite with internal circuit boards drawing 3W of power from a battery charged by the solar panels (false-color images labeled "3W Load", left, and indicated with solid and dotted red lines, right) are compared to the case where internal components are inactive (images labeled "No Load", left, and with thicker solid and dotted black lines, right).

the metallic satellite exterior surfaces. The dark regions in the upper half represent the smaller faces which receive little direct solar illumination during this given scenario. To better understand the contrast in EDF signature between

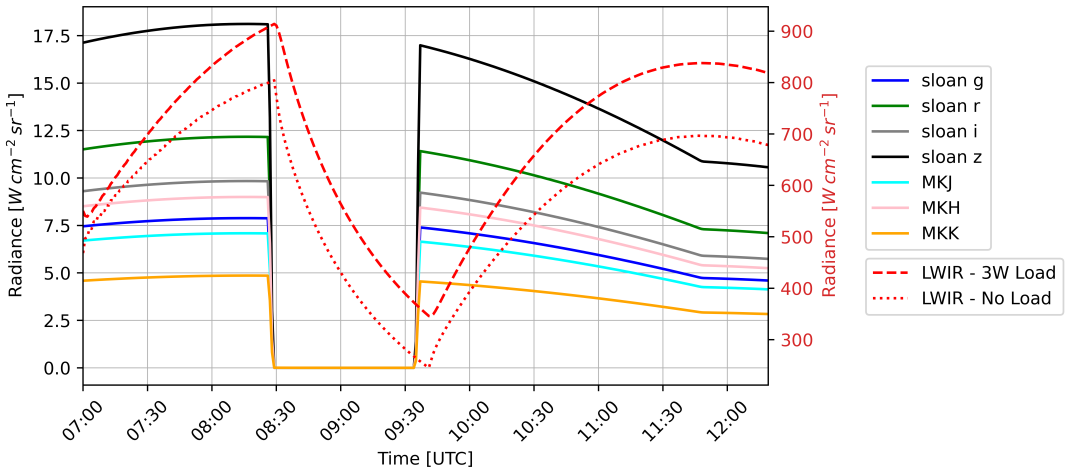

Fig. 17: Multi-spectral light curves for an Earth based sensor observing the 3U CubeSat model in the Scenario 3 orbit. Radiances in Sloan and Mauna Kea filter bands are solid lines and correspond to the left Y-axis. Radiance in LWIR for the two different operating loads correspond to the red-dotted lines and the right Y-axis.

the "3W Load" and "No Load" satellite, the difference of the two was computed and is presented in Figure 18 (c). The brightest regions from the EDF become brighter, where the radiance in the "3W Load" cases increases 3.7 $Wm^{-2}sr^{-1}$ for the NADIR face directed towards the sun.

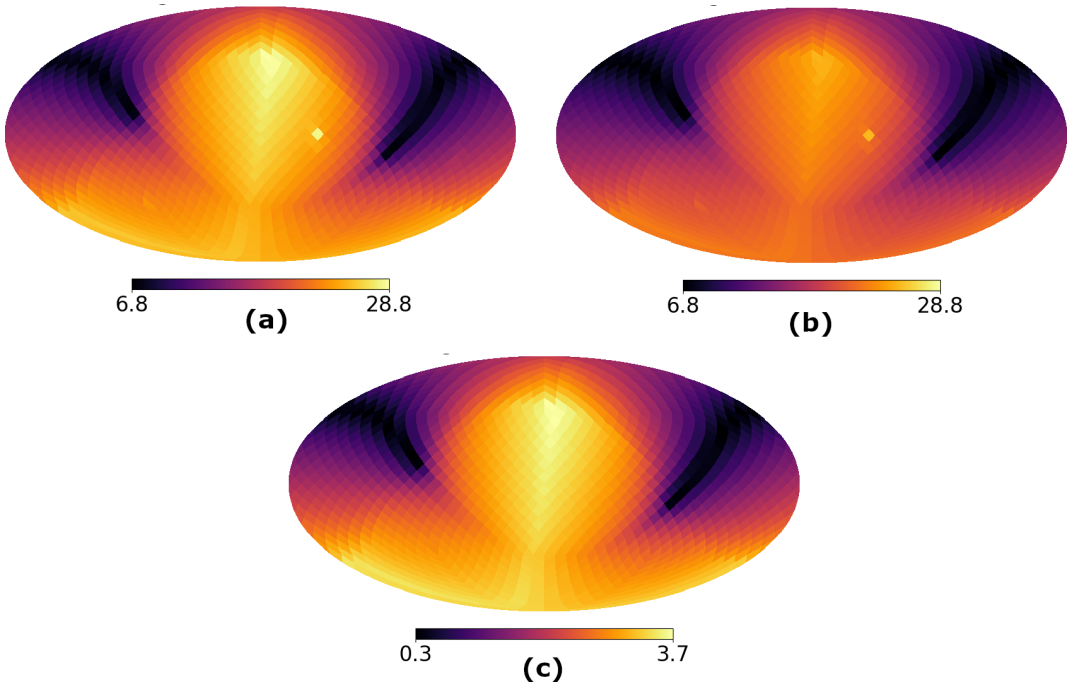

Fig. 18: Example EDF showing the directional radiance in units of $Wm^{-2}sr^{-1}$ for the GOES-17 scenario for a single time-step. Each point in the distribution represents an azimuth and elevation viewing angle. Azimuth angle starts at -180° on the left side of each plot and ends at 180° on the right side. Elevation is -90° at the bottom of the plot and 90° at the top. (a) GOES-17 EDF under a 3 watt load at 11:00 UTC. (b) GOES-17 EDF under no load at 11:00 UTC. (c) Difference between the EDF in (a) and (b) to show the predicted 3D signature difference between an orbiting satellite with an internal electronic load of 3W and an inactive satellite.

6. CONCLUSION

We have demonstrated the capability of using the commercial software MuSES™ for predicting surface temperatures of a 3U CubeSat operating at varying power loads in both LEO and GEO orbits. As we showed, by automatically coupling thermal and electrical solvers in a single transient simulation package with MuSES, temperature- and solar angle-dependent PV panel efficiency was calculated and used to predict the amount of harvested solar energy. This solar energy is used to power the electronic load of an orbiting satellite, and any excess energy charges the multi-cell battery pack. The battery pack, which charges when excess sunlight is present, discharges as necessary when the available PV-captured energy is insufficient for operational needs. This coupled thermal-electrical MuSES simulation results in the prediction of battery temperature, battery charge status (and even battery lifetime, if desired), solar panel temperatures and the temperature of all elements in the 3D model. Combined with spectral optical surface properties, EO/IR radiance predictions can be made by MuSES for a wide spectrum of band-integrated and hyperspectral sensors, with LWIR renderings being the focus of this work. Additionally, temperature results (stored in the MuSES TDF file format) can be read by other simulation packages when desired/necessary.

Temperature maps from MuSES in the form of TDF files were ingested by KODOS to extend its simulation environment to include thermal capabilities. KODOS demonstrated the ability to generate multi-spectral light curves in visible, SWIR and LWIR bands. Results show that, during eclipse periods, the radiance in the solar-dependent (short-wave) spectral bands falls off. In the LWIR, radiance values remain significant even during shadowed orbit segments but are temperature-dependent and thus decrease as the temperature of the CubeSat oscillates.

This work focused on a simple 3U CubeSat model but demonstrated the capability to integrate electronics, batteries and PVs. Future models will include additional passive and active thermal management components and other internal sources that may contribute to the overall thermal signature. For example, MuSES can activate heating elements (e.g., battery heaters) to keep sensitive components at stable temperatures in the absence of solar heating. In addition, other components such as magnetorquers or thrusters, heat pipes, deployable radiators, multi-layer insulation (MLI) blankets, sun-tracking PV panels and phase-change materials (PCM) can be included.

Photometric calibration of light curve data is a crucial step to producing meaningful data that can be used for analysis. Photometric calibration of LWIR data is difficult due to the lack of catalogued LWIR-band magnitudes. While temperatures can be estimated from LWIR data without photometric calibration by observing in two bands, atmospheric transmission and sky background are implicitly assumed to be identical between bands. While this may seem reasonable, any actual differences will yield a color error and an associated error in estimated temperature. The current methods for absolute flux calibration exploit combinations of calibration stars, blackbody sources, and sky subtraction, which may be weather and collection time dependent.

A candidate concept to mitigate calibration errors is to conduct LWIR observations with a co-boresighted VNIR camera, facilitating the use of Astrograph or astronomy.net to identify catalogued stars in the LWIR field. The spectral and luminosity class data can then be determined using spectral energy distribution (SED) fitting from model stellar atmospheres and star catalog magnitudes from a variety of bands. A tool such as SEDFitter [15] could be used to numerically fit a spectral distribution to these catalogue fluxes, which we anticipate can provide an estimate for the exo-atmospheric flux in the relevant LWIR band. Use of SEDFitter also allows simulations to be calibrated identically to observations, a capability we regard as key to successful use of simulation as a forward model.

7. ACKNOWLEDGEMENTS

The authors thank Eric Marttila, Derrick Levanen, Tim Viola, Zachary Edel, Jacob Hendrickson, Timofey Golubev, Eli Datema, Allison Edward, Logan Canull and Luke Marttila of ThermoAnalytics for their assistance during this effort.

8. REFERENCES

[1] Katelyn Elizabeth Boushon. *Thermal analysis and control of small satellites in low Earth orbit*. Missouri University of Science and Technology, 2018.

[2] Scott D Brown and John R Schott. Verification and validation studies of the dirsig data simulation model. *Rochester Institute of Technology, Rochester, NY, USA, Tech. Rep*, 1(6), 2010.

[3] Robert Crow, Kathy Crow, Richard Preston, and Elizabeth Beecher. Hyperspectral measurements of space objects with a small format sensor system. In *Advanced Maui Optical and Space Surveillance (AMOS) Technologies Conference*, page 61, 2017.

[4] Ahmed Elhefnawy, Ali Elmaihy, and Ahmed Elweteedy. Passive thermal control design and analysis of a university-class satellite. *Journal of Thermal Analysis and Calorimetry*, 147(23):13633–13651, 2022.

[5] Emanuel Escobar, Marcos Diaz, and Juan Cristóbal Zagal. Evolutionary design of a satellite thermal control system: Real experiments for a cubesat mission. *Applied Thermal Engineering*, 105:490–500, 2016.

[6] Alejandro Garzón and Yovani A Villanueva. Thermal analysis of satellite Libertad 2: A guide to CubeSat temperature prediction. *Journal of Aerospace Technology and Management*, 10:e4918, 2018.

[7] Timofey Golubev and Richard R Lunt. Evaluating the electricity production of electric vehicle-integrated photovoltaics via a coupled modeling approach. In *2021 IEEE 48th Photovoltaic Specialists Conference (PVSC)*, pages 0155–0159. IEEE, 2021.

[8] Doyle Hall, John Africano, David Archambeault, Brian Birge, David Witte, and Paul Kervin. Amos observations of nasa's image satellite. In *The 2006 AMOS Technical Conference Proceedings*, pages 10–14, 2006.

[9] Doyle Hall, Paul Kervin, Andrew Nicholas, Jake Griffiths, Ivan Galysh, and Michael Werth. Multi-sensor observations of the spinsat satellite. In *Advanced Maui Optical and Space Surveillance Technologies Conference*, page 66, 2015.

[10] Derek Hengeveld and Jacob Moulton. Automatic creation of reduced-order models using Thermal Desktop. 48th International Conference on Environmental Systems, 2018.

[11] M. Klein, P. Rynes, A. Ifarraguerri, T. Anderson, and G. Whittier. Validation of a MWIR and LWIR MuSES signature model of a camouflage net. In *Proc. of the MSS Specialty Group on Battlefield Survivability and Discrimination*. SENSIAC, GTARC, Atlanta, GA, 2012.

[12] Scott Peck, Theodore Olszanski, Sonya Zanardelli, and Matt Pierce. Validation of a thermal-electric li-ion battery model. *SAE International Journal of Passenger Cars-Electronic and Electrical Systems*, 5(2012-01-0332):154–163, 2012.

[13] Scott Peck and Matt Pierce. Development of a temperature-dependent li-ion battery thermal model. Technical report, SAE Technical Paper, 2012.

[14] Scott Peck, Aditya Velivelli, and Wilko Jansen. Options for coupled thermal-electric modeling of battery cells and packs. *SAE International Journal of Passenger Cars-Electronic and Electrical Systems*, 7(2014-01-1834):273–284, 2014.

[15] Thomas P. Robitaille, Barbara A. Whitney, Remy Indebetouw, and Kenneth Wood. Interpreting Spectral Energy Distributions from Young Stellar Objects. II. Fitting Observed SEDs Using a Large Grid of Precomputed Models. *The Astrophysical Journal Supplement Series*, 169(2):328–352, April 2007.

[16] P. Rynes, M. Klein, C. Packard, D. Less, T. Viola, and P. Capuzzi. A model-based system to evaluate the EOIR signature of special operations forces. In *Proc. of the MSS Specialty Group on Battlefield Survivability and Discrimination*. SENSIAC, GTARC, Atlanta, GA, 2014.

[17] Kameron Simon, Steve Williams, and Ian Hersom. Passive RF in support of LEO orbit determination. In *2022 Advanced Maui Optical and Space Surveillance Technologies Conference (AMOS)*, 2022.

[18] David W Tyler and Casey Demars. Airlight-imposed errors for space-object polarimetric observations from the ground. *Applied Optics*, 57(9):2235–2244, 2018.

[19] David Vallado, Paul Crawford, Richard Hujsak, and TS Kelso. Revisiting spacetrack report# 3. In *AIAA/AAS Astrodynamics Specialist Conference and Exhibit*, page 6753, 2006.

[20] Michael Werth, Brandoch Calef, Daniel Thompson, and Lisa Thompson. Fusing lwir data and visible imagery with multi-frame blind deconvolution. In *2016 IEEE Aerospace Conference*, pages 1–10. IEEE, 2016.

[21] Charles J Wetterer and Moriba Jah. Attitude determination from light curves. *Journal of Guidance, Control, and Dynamics*, 32(5):1648–1651, 2009.